

Terahertz-Range Polar Modes in Domain-Engineered BiFeO₃

Jirka Hlinka,* Marek Paściak, Sabine Körbel, and Pavel Marton

Institute of Physics, Academy of Sciences of the Czech Republic, Na Slovance 2, 182 21 Prague 8, Czech Republic

(Received 2 March 2017; published 4 August 2017)

The dielectric permittivity and properties of electrically active lattice resonances in nanotwinned BiFeO₃ crystals have been studied theoretically using an earlier established interatomic potential. The results suggest that an array of 71° domain walls with about 2–5 nm spacing enhances the static permittivity of BiFeO₃ by more than an order of magnitude. This enhancement is associated with an electrically active excitation, corresponding to a collective vibration of pinned domain walls at a remarkably high frequency of about 0.3 THz.

DOI: 10.1103/PhysRevLett.119.057604

Nanoscale ferroelectric domains are readily encountered in various materials. Their occurrence can be favored by the chemical composition [1,2] or the grain size [3,4] in polycrystals and they often occur in ferroelectric thin films [5–11] and superlattices [12,13]. The high density of domain walls may increase useful functional properties of the twinned materials [7,14,15]. For example, it has been argued that it may lead to an enhancement of the dielectric permittivity [14,16–19], the piezoelectric properties [20–23], or the photovoltaic properties [24–26].

As a material combining strong ferroelectricity, oxygen octahedra tilt distortions, and magnetic ordering, BiFeO₃ became a favorite subject for investigating various structure-property relationships [10,27–31]. Moreover, it is one of the model materials in which regular arrays of domain walls have been already prepared using methods of contemporary thin-film technology [7,9,32]. Thin films with arrays of parallel 71° domain walls [7,24,32,33] as well as thin films with arrays of 109° domain walls [24,32,34,35] have been prepared in the past. A regular array of 100 nm thick domains separated by 71° domain walls actually shows very peculiar photovoltaic properties of BiFeO₃ that scale with the density of domain walls [24,25].

In order to learn more about the nanotwinned BiFeO₃, we have performed calculations of the dielectric properties of BiFeO₃ with regular arrays of 180°, 109°, and 71° domain walls with spacings of about 2–10 nm, using a material-specific atomistic model (see Fig. 1). In the case of 71° twinning, a sizable enhancement of the overall macroscopic dielectric permittivity is found. While the usual dielectric contributions of pinned ferroelectric domain walls are normally associated with MHz and GHz-range resonances, here the enhancement is due to a THz-range polar vibration of the 71° domain walls.

In this work we use a classical shell model, in which each atom is represented by coordinates of its core and shell, simulating an atomic nucleus with core electrons and the valence electronic cloud, respectively [37,38]. The

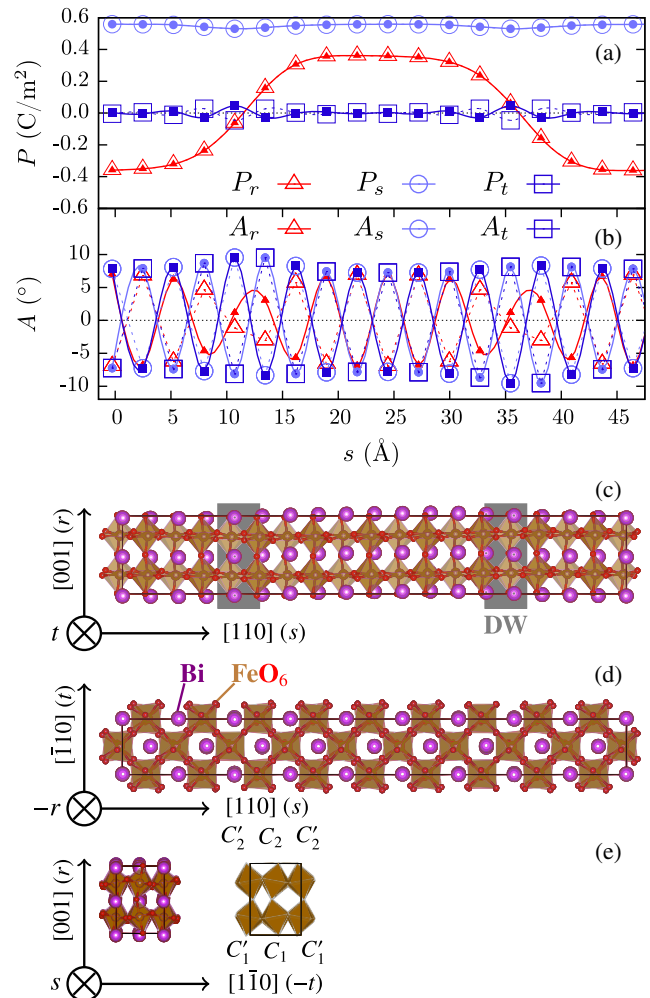


FIG. 1. Shell-model-optimized 180-atom supercell with two 71° domain walls. The top panel shows profiles of order parameter components, the bottom panels show the real atomic structure. Solid symbols: Octahedral chains C_1 and C'_1 depicted in (e), open symbols: C_2 and C'_2 . The description includes the adopted axis notation, where r is the direction in which the polarization changes sign across the domain wall, s is normal to the domain wall plane, and t is normal to r and s [36].

interatomic potential involves interaction terms with numerical coefficients determined for BiFeO₃ by Graf *et al.* [39], using fully *ab initio* density-functional theory calculations. The potential includes (i) the electrostatic energy of the point charges attached to each core and shell, (ii) the intra-atomic interaction $V(\omega) = 1/2k_2\omega^2 + 1/24k_4\omega^4$, where ω is the core-shell displacement, (iii) Rydberg potentials $V(r) = (a + Br)\exp(-r/\rho)$ among all shells up to a cutoff radius of 7.2 Å, and (iv) the Fe-O-Fe bond-bending term $V(\theta) = 1/2k_B[\cos(\theta) - \cos(\theta_B)]^2$. This model was already used in Refs. [39–41].

All structure optimizations, lattice dynamics, and dielectric tensor calculations were done with the program GULP [42]. Our single-domain structure and spontaneous polarization are in reasonable agreement with earlier findings [39–41], and the single-domain permittivity from our linear response calculations, $\epsilon_{11} = \epsilon_{22} = 23$ and $\epsilon_{33} = 19$, is not far from the values $\epsilon_{11} = \epsilon_{22} = 36$ and $\epsilon_{33} = 23$ obtained from finite-temperature molecular dynamics simulations of Ref. [40].

Having a cubic perovskite parent phase, the rhombohedral ferroelectric *R3c* phase of BiFeO₃ allows for 180°, 109°, and 71° twins [43,44], associated with the $m\bar{3}m > 3m$ macroscopic symmetry reduction (species No. 186 of Ref. [45]). The energies of the various possibilities of twin boundaries, differing by their crystallographic orientations and the concurrent oxygen octahedra tilt patterns, have been thoroughly investigated in Ref. [46]. Here we consider only the three lowest-energy configurations of the three prominent mechanically and electrically compatible domain walls, denoted in Table III of Ref. [46] as $[1\bar{1}\bar{1}](110)[\bar{1}\bar{1}\bar{1}]$ 3/0, $[111](100)[\bar{1}\bar{1}\bar{1}]$ 2/1, $[111](110)[\bar{1}\bar{1}\bar{1}]$ 1/1, and here for brevity just as the 180°, 109°, and 71° domain walls, respectively.

An example of a supercell with two 71° domain walls, showing the atomic positions relaxed within the shell model, is shown in Fig. 1. For clarity, we also display there the resulting polarization and oxygen octahedra tilt profiles. Here, the local dipole moment was evaluated for each five-atom unit cell centered on the Fe ion [47]. Note that we systematically employ the Cartesian system r , s , t related to the ferroelectric domain-wall geometry, in which s is along the domain-wall normal and r is directed along the switched polarization component [36].

To compare with the results of Ref. [46], we have first optimized the equivalent 120, atom supercells. The shell-model optimizations yielded similar stable atomic configurations and a similar hierarchy of domain-wall energies (shell-model planar energy densities of 72, 29, and 125 mJ/m² of the 180°, 109°, and 71° domain walls correspond to *ab initio* values of 74, 62, and 152 mJ/m² in Ref. [46], respectively). This energy hierarchy nicely relates to the fact that the 109° domain walls are most frequently found in BiFeO₃ bulk materials [48,49].

Direct permittivity calculations [42] for the 120-atom supercell with a pair of domain walls reveal the expected

moderate enhancement of the permittivity in the case of 109° domain walls (the highest component of the permittivity tensor is $\epsilon_{rr} \approx 30$) as well as for the 180° domain walls ($\epsilon_{rr} \approx 30$ and $\epsilon_{tt} \approx 40$). For the supercell with two 71° domain walls, ϵ_{rr} attains a considerable magnitude of $\epsilon_{rr} \approx 170$. We then explored a range of domain-wall distances and realized that a 180-atomic cell with two 71° domain walls shows a yet bigger ϵ_{rr} of ≈ 650 .

Where does this enhancement come from? In principle, the static permittivity can be expressed in terms of individual contributions of infrared-active (polar) excitations of the system through the generalized Lyddane-Sachs-Teller relation [50]. In our model, such excitations can be considered as polar zone-center modes of the whole supercell, and their spectrum can be calculated with standard methods [42]. The frequency dependence of the real and the imaginary part of the principal components of the dielectric permittivity tensor calculated with a damping factor of 2 cm⁻¹ for the 180-atom cell is shown in Fig. 2. The comparison with single-domain spectra immediately reveals that there is one very strong additional mode at about 12 cm⁻¹ in the ϵ_{rr} spectrum of the supercell with 71° domain walls (mode denoted as A in Fig. 2), which is responsible for most of the detected static permittivity enhancement. Note that the stronger modes above 75 cm⁻¹, such as the modes denoted as C and D, have their trivial counterparts in the single-domain spectra, and so it is clear that none of them can cause the drastic permittivity enhancement.

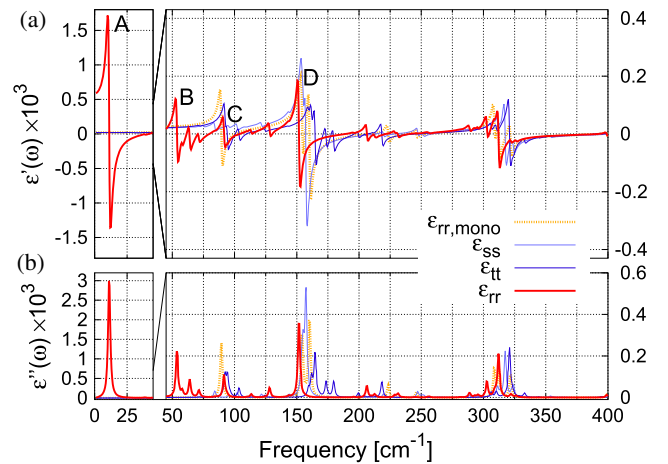


FIG. 2. Real (a) and imaginary (b) part of the principal components of the frequency-dependent permittivity of BiFeO₃ with 71° domain walls (calculated for the supercell shown in Fig. 1). A damping factor of 2 cm⁻¹ has been used. For comparison, the diagonal element of the monodomain permittivity tensor corresponding to the direction r of the supercell with domain walls is also shown. Two different vertical scales were applied in order to better visualize the higher-frequency signal. The letters A, B, C, and D mark resonances of ϵ_{rr} that are further discussed in the text.

The multiple new modes contributing to the permittivity spectra are related to the reduction of the translational symmetry in the direction perpendicular to the domain walls. In order to relate the individual polar modes to the modes of the parent cubic perovskite lattice [51], we have unfolded the phonon dispersion curves of the supercell within the Brillouin zone of the parent cubic phase (Fig. 3).

For this purpose, we have explored zone-center modes of extended supercells with multiple equidistant domain walls. Their eigenmodes were projected on auxiliary Bloch lattice waves, indexed by wave vectors of the $\Gamma - M$ line in the first Brillouin zone of the parent cubic perovskite reference structure, directed along the domain-wall normal. Since all polar modes in this frequency region have dominantly Last-type character, the auxiliary Bloch modes were constructed only with the ideal Last-type eigenvector [52] (the polar mode involving antiphase beating of the Bi ion against rigid FeO_3 octahedra). Using only its r component allows us to highlight the modes related to ϵ_{rr} .

Technically, the participation ratio in the auxiliary Bloch state with a selected wave vector \mathbf{q} was calculated for each of the zone-center modes of a 8×180 -atom supercell with frequency ν . The resulting weights, smoothed by a broadening factor $\sigma = 2 \text{ cm}^{-1}$, were summed up into the integral function

$$I(\mathbf{q}, \nu) = \sum_k^{3N} \exp\left(-\frac{(\nu - \nu_k)^2}{\sigma^2}\right) \left| \sum_j^N W_j \exp(i\mathbf{q} \cdot \mathbf{r}_j) \xi_k^r \right|^2, \quad (1)$$

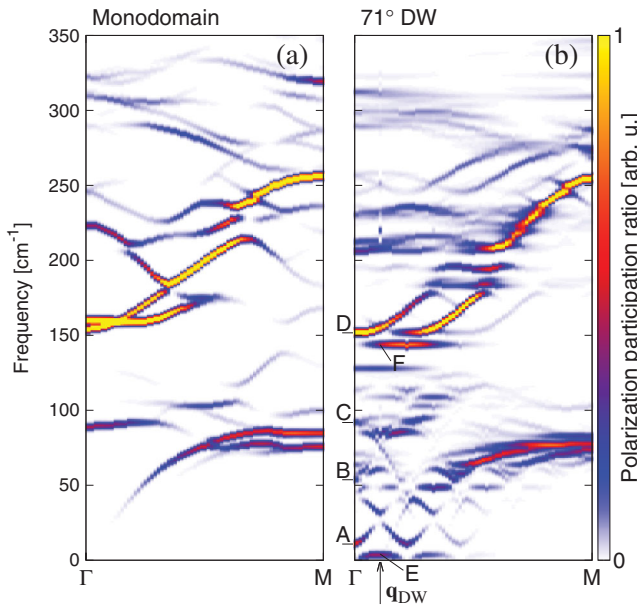


FIG. 3. Dispersion curves calculated for the monodomain [(a), left] and 71° domain wall [(b), right] structure of Fig. 1. The color scale indicates the projection onto the r component of the Last-type mode with the wave vector \mathbf{q} along the s direction, with hotter colors marking a bigger participation ratio.

where the first sum runs over all eigenmodes k and the second over all atoms j , \mathbf{r} is the position of an atom in the structure, ξ is the eigenvector, and W_j is the Last-mode related weight [52] depending on the atomic masses m_{Pb} , m_{Fe} , and m_{O} as $W_j = -1/\sqrt{m_{\text{Pb}}}$, $W_j = \sqrt{m_{\text{Fe}}}/(m_{\text{Fe}} + 3m_{\text{O}})$ and $W_j = \sqrt{m_{\text{O}}}/(m_{\text{Fe}} + 3m_{\text{O}})$ for Pb, Fe, and O atoms, respectively. This function is displayed in Fig. 3.

For comparison, a likewise calculated dispersion, but for a monodomain, oriented as one of the domain states considered, is shown in Fig. 3(a). On both panels, one can clearly see the trace of the original Last-type phonon branch there, connecting the zone-center polar mode near $\approx 150 \text{ cm}^{-1}$ with the corresponding zone-boundary mode near $\approx 250 \text{ cm}^{-1}$. The additional branches in Fig. 3(a) reflect the usual mode hybridization associated with the difference between the monodomain ferroelectric and the parent cubic state. In particular, the lowest-frequency zone-center mode near $\approx 90 \text{ cm}^{-1}$ originates from the frozen antidistortive mode, documented experimentally [29,53].

Dispersion curves of the nanotwinned supercell [Fig. 3(b)] are much more fragmented. Most important are the lowest-frequency excitations, absent in Fig. 3(a). The dispersion curve connected to the mode A shows a pronounced reciprocal-space periodicity corresponding to the $2w_d$ real-space periodicity set by the domain-wall (DW) distance $w_d = 9a_0(1 + u_{ss})/\sqrt{2}$, where a_0 is the parent lattice constant and u_{ss} is the supercell elongation relative to its cubic-phase length along the s direction. At the corresponding reciprocal lattice point $\mathbf{q}_{\text{DW}} = (1, 1, 0)\pi/(\sqrt{2}w_d)$, the participation ratio of this branch is vanishing. It indicates that the corresponding weight is transformed to the nearby mode E, attached to the acoustic branch. The marked dispersion gap at the \mathbf{q}_{DW} point suggests strong interaction of these branches with the domain walls.

It is worth mentioning that the periodic sequence of domain walls can be considered a long-period, commensurately modulated structure with the modulation wave vector \mathbf{q}_{DW} [54–56]. In the case of incommensurately modulated phases, a rigid shift of the polarization profile along \mathbf{q}_{DW} does not change the overall energy, and this often results in the appearance of a gapless homogeneous phason mode, corresponding to such shift [54–56]. In the case of a commensurate phase, a nonzero gap develops on the phason branch. In fact, the two dispersion curves attached to modes A and E strongly resemble the coupled acoustic–phason branches, known from incommensurate structures [54–56], and it can be thus guessed that the modes A and E are the inhomogeneous [57] and homogeneous phason modes, respectively [58,59].

The calculated mode eigenvectors allow to inspect their involvement in polarization fluctuations at the scale of individual perovskite unit cells. Figure 4 shows the dynamical polarization profiles of selected modes, calculated from their eigenvectors. The dynamical pattern of these modes has the same period as that of the static

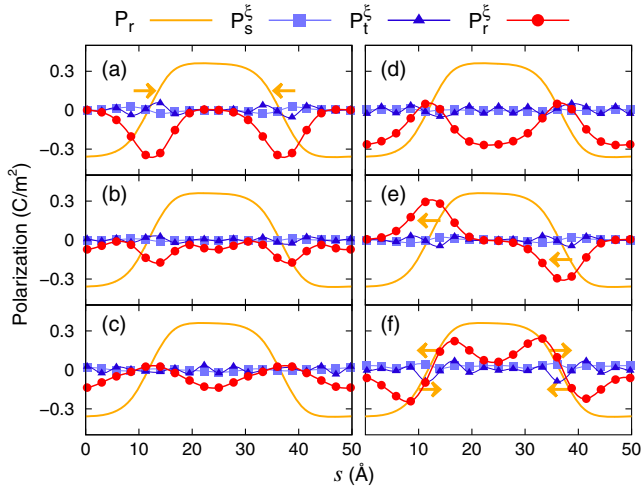


FIG. 4. The dynamical polarization profiles associated with the modes marked in Figs. 2, 3. Each point symbol marks a polarization component (squares, s ; triangles, t ; and circles, r direction) calculated from mode eigenvectors [47]. The static polarization profile P_r is the same as in Fig. 1. Arrows mark wall movements caused by a particular mode. The panels (a)–(f) refer to modes marked A–F in Fig. 2b.

polarization. The static and dynamic polarization profiles are shown only for two rows of oxygen octahedra.

The underlying domain structure is best reflected in the r component of their polarization profiles. Mode D , related to the Last-type zone-center mode of the monodomain state, shows uniform fluctuations within domains. Weak modes B and C have similar polarization profiles to A and D , respectively, suggesting a mode mixing [56].

The high-permittivity mode A involves primarily polarization displacements localized at the domain wall. These displacements involved can be interpreted as a shift of the domain wall along the domain-wall normal. Adjacent domain walls are shifted in opposite directions, so that the total polarization is showing large fluctuations in time. This confirms that this mode is the equivalent of the inhomogeneous infrared-active phason [57], investigated in incommensurate crystals [55,58]. In opposition to mode A , the eigenvector of the mode E involves domain wall shifts in the same sense, so that the polarization profile is sliding as a whole (homogeneous phason). Here the total polarization is conserved, the mode is nonpolar. The nearly dispersionless mode F involves also fluctuations located at domain walls, but there its profile resembles the second derivative of the static polarization, and it can be thus interpreted as the wall thickness-breathing mode [60,61].

As the domain-wall distances are increasing above about 3 nm, the permittivity gradually falls down and the frequency ν_A of the mode A decreases towards that of mode E , while the latter (ν_E) does not change appreciably. In fact, the difference $\nu_A^2 - \nu_E^2$ can be ascribed to the domain-wall repulsion caused by elastic energy [62]. More interestingly, the THz-range frequency of the phason

gap ($\nu_E \approx 5 \text{ cm}^{-1} \approx 0,1 \text{ THz}$) suggests an intrinsic pinning of these domain walls.

Such an intrinsic domain wall pinning can be very surprising at first sight, because the Peierls-Nabarro barrier for a ferroelectric domain wall thicker than two perovskite unit cells is known to be very small [63], and here the thickness of the investigated 71° wall is about 1 nm. However, it should be understood that in BiFeO_3 , the polarization profile is primarily coupled to the oxygen octahedra tilt profile. The sign of the local tilt angles alternates between the adjacent unit cells, so that the oxygen octahedra tilt profile is rather efficiently pinned to the crystal lattice. Since the coupling between the polarization and tilt (polar and axial vector) is by its nature indifferent to the sense of the tilt angle, the easy axis direction for the polarization as well as the polarization itself may vary smoothly when passing from cell to cell. When the tilt axis profile is spread over several atomic layers, as within the 71° domain wall, the polarization profile is necessarily broadened, too. We believe that the overall strength of this mixed pinning mechanism and the intrinsic thickness of the tilt profile primarily determine together the strength and THz-range frequency of the observed infrared-active phason mode.

This picture also allows us to explain why a similar enhancement is not expected in the case of 180° and 109° domain walls. The 109° domain wall has, in contrast to the 71° one, a rather narrow kink of the tilt-vector profile. This is certainly related to the fact that the tilt pattern of adjacent domain states can be in principle matched at a single atomic layer without any distortion of the oxygen octahedra, as discussed in [46]. This also holds for the case of the studied 180° domain wall (there is practically no variation of the tilt axis across the wall). In this sense, the 71° domain wall is very peculiar case—the above described domain wall broadening caused by the underlying broad tilt profile is not present in the other two domain walls. Since the domain-wall widths of the 109° and 180° domain walls are smaller than the lattice period, we do not expect the THz-frequency phason mode there. This is indeed verified by a direct inspection of the dispersion curves of lattice vibrations in the supercells with 180° and 109° domain walls [64].

In summary, we have studied domain structures of BiFeO_3 in the framework of *ab-initio* based shell model and seen that it gives realistic predictions. A peculiar increase of the dielectric permittivity has been noticed for a dense system of 71° domain walls with domain-wall distances of about 2–5 nm. We developed a computationally feasible scheme allowing insight into the dynamics of such domain walls and their contribution to the permittivity. Frequencies of the phason and wall-broadening modes were estimated without necessity to introduce additional phenomenological parameters. The permittivity increase encountered in the case of 71° domain walls was shown to

be related to a THz-range infrared-active mode, representing specific concerted domain-wall vibrations. The THz-range frequency of this mode reflects an unusual pinning mechanism of the 71° domain walls of BiFeO_3 , involving the coupling between the polarization and antiferrodistortive order parameters. We believe that the dielectric spectrum of this mode might be probed with contemporary THz-spectroscopy techniques. Therefore, all our results suggest that it is worth the effort to prepare and study THz-range properties of BiFeO_3 thin films or superlattices with a high density of 71° domain walls.

This work is supported by the Czech Science Foundation (Project No. 15-04121S).

*hlinka@fzu.cz

- [1] S.-E. Park and T. R. ShROUT, *J. Appl. Phys.* **82**, 1804 (1997).
- [2] T. Asada and Y. Koyama, *Phys. Rev. B* **75**, 214111 (2007).
- [3] A. Pramanick, A. D. Prewitt, J. S. Forrester, and J. L. Jones, *Crit. Rev. Solid State Mater. Sci.* **37**, 243 (2012).
- [4] L. M. Eng, H.-J. Güntherodt, G. A. Schneider, U. Köpke, and J. M. Saldaña, *Appl. Phys. Lett.* **74**, 233 (1999).
- [5] A. Schilling, T. B. Adams, R. M. Bowman, J. M. Gregg, G. Catalan, and J. F. Scott, *Phys. Rev. B* **74**, 024115 (2006).
- [6] S. K. Streiffer, J. A. Eastman, D. D. Fong, C. Thompson, A. Munkholm, M. V. Ramana Murty, O. Auciello, G. R. Bai, and G. B. Stephenson, *Phys. Rev. Lett.* **89**, 067601 (2002).
- [7] Z. Chen, J. Liu, Y. Qi, D. Chen, S.-L. Hsu, A. R. Damodaran, X. He, A. T. N'Diaye, A. Rockett, and L. W. Martin, *Nano Lett.* **15**, 6506 (2015).
- [8] L. Feigl, P. Yudin, I. Stolichnov, T. Sluka, K. Shapovalov, M. Mtebwa, C. S. Sandu, X.-K. Wei, A. K. Tagantsev, and N. Setter, *Nat. Commun.* **5**, 4677 (2014).
- [9] G. Pan, W. Wen, X. Li, Q. He, T. Sriharan, Y. H. Chu, L. Chen, and C. Gao, *Phys. Rev. B* **88**, 064103 (2013).
- [10] G. Catalan, H. Béa, S. Fusil, M. Bibes, P. Paruch, A. Barthélémy, and J. F. Scott, *Phys. Rev. Lett.* **100**, 027602 (2008).
- [11] B. Ziegler, K. Martens, T. Giamarchi, and P. Paruch, *Phys. Rev. Lett.* **111**, 247604 (2013).
- [12] P. Zubko, J. C. Wojdeł, M. Hadjimichael, S. Fernandez-Pena, A. Sené, I. Luk'yanchuk, J.-M. Triscone, and J. Íñiguez, *Nature (London)* **534**, 524 (2016).
- [13] G. Rispens, B. Ziegler, Z. Zanolli, J. Íñiguez, P. Ghosez, and P. Paruch, *Phys. Rev. B* **90**, 104106 (2014).
- [14] A. K. Tagantsev, L. E. Cross, and J. Fousek, *Domains in Ferroic Crystals and Thin Films* (Springer, New York, 2010).
- [15] V. A. Stephanovich, I. A. Luk'yanchuk, and M. G. Karkut, *Phys. Rev. Lett.* **94**, 047601 (2005).
- [16] I. Luk'yanchuk, A. Pakhomov, A. Sené, A. Sidorkin, and V. Vinokur, *arXiv:1410.3124*.
- [17] Li Jin, V. Porokhonsky, and D. Damjanovic, *Appl. Phys. Lett.* **96**, 242902 (2010).
- [18] Y. L. Wang, A. K. Tagantsev, D. Damjanovic, and N. Setter, *Appl. Phys. Lett.* **91**, 062905 (2007).
- [19] S. Liu and R. E. Cohen, *Phys. Rev. B* **95**, 094102 (2017).
- [20] S. Zhang and F. Li, *J. Appl. Phys.* **111**, 031301 (2012).
- [21] J. Hlinka, P. Ondrejovic, and P. Marton, *Nanotechnology* **20**, 105709 (2009).
- [22] E. Sun and W. Cao, *Prog. Mater. Sci.* **65**, 124 (2014).
- [23] T. Rojac, A. Bencan, G. Drazic, M. Kosec, and D. Damjanovic, *J. Appl. Phys.* **112**, 064114 (2012).
- [24] J. W. Ager, III, L. W. Martin, and R. Ramesh, *Nat. Nanotechnol.* **5**, 143 (2010).
- [25] H. Matsuo, Y. Kitanaka, R. Inoue, Y. Noguchi, M. Miyayama, T. Kiguchi, and T. J. Konno, *Phys. Rev. B* **94**, 214111 (2016).
- [26] R. Inoue, S. Ishikawa, R. Imura, Y. Kitanaka, T. Oguchi, Y. Noguchi, and M. Miyayama, *Sci. Rep.* **5**, 14741 (2015).
- [27] R. Ramesh and N. A. Spaldin, *Nat. Mater.* **6**, 21 (2007).
- [28] G. Catalan and J. F. Scott, *Adv. Mater.* **21**, 2463 (2009).
- [29] J. Hlinka, J. Pokorny, S. Karimi, and I. M. Reaney, *Phys. Rev. B* **83**, 020101(R) (2011).
- [30] J. C. Yang, Y. L. Huang, Q. He, and Y. H. Chu, *J. Appl. Phys.* **116**, 066801 (2014).
- [31] D. Sando, A. Barthélémy, and M. Bibes, *J. Phys. Condens. Matter* **26**, 473201 (2014).
- [32] Y.-H. Chu, Q. He, C.-H. Yang, P. Yu, L. W. Martin, P. Shafer, and R. Ramesh, *Nano Lett.* **9**, 1726 (2009).
- [33] S. Farokhipoor and B. Noheda, *Phys. Rev. Lett.* **107**, 127601 (2011).
- [34] A. Crassous, T. Sluka, C. S. Sandu, and N. Setter, *Ferroelectrics* **480**, 41 (2015).
- [35] J. Seidel, G. Singh-Bhalla, Q. He, S.-Y. Yang, Y.-H. Chu, and R. Ramesh, *Phase Transitions* **86**, 53 (2013).
- [36] P. Marton, I. Rychetsky, and J. Hlinka, *Phys. Rev. B* **81**, 144125 (2010).
- [37] R. Migoni, H. Bilz, and D. Bäuerle, *Phys. Rev. Lett.* **37**, 1155 (1976).
- [38] B. G. Dick, Jr. and A. W. Overhauser, *Phys. Rev.* **112**, 90 (1958).
- [39] M. Graf, M. Sepliarsky, S. Tinte, and M. G. Stachiotti, *Phys. Rev. B* **90**, 184108 (2014).
- [40] M. Graf, M. Sepliarsky, R. Machado, and M. G. Stachiotti, *Solid State Commun.* **218**, 10 (2015).
- [41] M. Graf, M. Sepliarsky, and M. G. Stachiotti, *Phys. Rev. B* **94**, 054101 (2016).
- [42] J. D. Gale and A. L. Rohl, *Mol. Simul.* **29**, 291 (2003).
- [43] J. Fousek and V. Janovec, *J. Appl. Phys.* **40**, 135 (1969).
- [44] M. Taherinejad, D. Vanderbilt, P. Marton, V. Stepkova, and J. Hlinka, *Phys. Rev. B* **86**, 155138 (2012).
- [45] J. Hlinka, J. Privratska, P. Ondrejovic, and V. Janovec, *Phys. Rev. Lett.* **116**, 177602 (2016).
- [46] O. Diéguez, P. Aguado-Puente, J. Junquera, and J. Íñiguez, *Phys. Rev. B* **87**, 024102 (2013).
- [47] Assuming nominal ionic charges Bi^{3+} , Fe^{3+} , and O^{2-} .
- [48] F. Borodavka, J. Pokorny, and J. Hlinka, *Phase Transitions* **89**, 746 (2016).
- [49] A. Sander, M. Christl, C.-T. Chiang, M. Alexe, and W. Widdra, *J. Appl. Phys.* **118**, 224102 (2015).
- [50] R. H. Lyddane, R. G. Sachs, and E. Teller, *Phys. Rev.* **59**, 673 (1941).
- [51] P. Ghosez, E. Cockayne, U. V. Waghmare, and K. M. Rabe, *Phys. Rev. B* **60**, 836 (1999).
- [52] J. Hlinka, J. Petzelt, S. Kamba, D. Noujni, and T. Ostapchuk, *Phase Transitions* **79**, 41 (2006).

- [53] E. Borissenko, M. Goffinet, A. Bosak, P. Rovillain, M. Cazayous, D. Colson, P. Ghosez, and M. Krisch, *J. Phys. Condens. Matter* **25**, 102201 (2013).
- [54] R. Currat and T. Jansen, *Solid State Physics 41* (Academic Press, New York, 1988).
- [55] D. G. Sannikov, *Incommensurate Phases in Dielectrics 14.1 Fundamentals* (North Holland, Amsterdam, 1986).
- [56] J. Hlinka, M. Quilichini, R. Currat, and J. F. Legrand, *J. Phys. Condens. Matter* **9**, 1461 (1997).
- [57] J. Hlinka, J. Petzelt, B. Březina, and R. Currat, *Phys. Rev. B* **66**, 132302 (2002).
- [58] J. Hlinka, M. Iwata, and Y. Ishibashi, *J. Phys. Soc. Jpn.* **68**, 126 (1999).
- [59] J. Ollivier, J. Etrillard, B. Toudic, C. Ecolivet, P. Bourges, and A. P. Levanyuk, *Phys. Rev. Lett.* **81**, 3667 (1998).
- [60] W.-F. Rao and Y. U. Wang, *Appl. Phys. Lett.* **90**, 041915 (2007).
- [61] X. Wu, U. Petralanda, L. Zheng, Y. Ren, R. Hu, S.-W. Cheong, S. Artyukhin, and K. Lai, *Sci. Adv.* **3**, e1602371 (2017).
- [62] G. Arlt and N. A. Pertsev, *J. Appl. Phys.* **70**, 2283 (1991).
- [63] B. Meyer and D. Vanderbilt, *Phys. Rev. B* **65**, 104111 (2002).
- [64] See Supplemental Material at <http://link.aps.org/supplemental/10.1103/PhysRevLett.119.057604> for dispersion curves of the other two domain walls.